

## APPLIED PHYSICS

# Broadband photodetection of intense lasers via exciton-enhanced high-order multiphoton-absorption optoelectronics in 2D hybrid perovskite

Yanming Xu<sup>1,2†</sup>, Haojie Xu<sup>3†</sup>, Pengfei Zhu<sup>3</sup>, Jinlong Xu<sup>1,2\*</sup>, Yantang Huang<sup>1</sup>, Zhihua Sun<sup>3\*</sup>, Fushan Li<sup>1\*</sup>, Shining Zhu<sup>2</sup>, Lin Zhou<sup>2\*</sup>

Broadband photodetection, especially for the high-intensity pulsed lasers, has garnered increasing interest in photophysics and applied sciences driven by the development of pulsed lasers. However, direct broadband photodetection of high-intensity pulsed lasers, with precisely capturing their spatiotemporal properties, has been hampered by low saturation intensity or damage threshold of traditional optoelectronic materials. Here, we demonstrate that strategic enhancement of excitonic effects in two-dimensional (2D) layered hybrid perovskite can enable robust high-order multiphoton absorption (MPA) optoelectronics with achieving strong four-photon absorption (4PA) and five-photon absorption (5PA) nonlinearities as well as efficient electronic properties simultaneously. This effectively overcomes the limitations of mainstream photodetectors. Our approach facilitates direct photodetection and high-precision imaging of high-intensity femtosecond lasers (21.5 GW/cm<sup>2</sup>) across a broad wavelength range of 800 to 2300 nanometer. These results offer valuable insights into advancing high-order nonlinearity-based optoelectronics and provide practical solutions for direct measurement tools of intensive lasers, filling the blank of high-precision characterization of intense-field laser phenomena.

## INTRODUCTION

Since the invention of Ti:sapphire femtosecond (fs) laser (1), high-intensity pulsed lasers have been recognized as revolutionary tools enabling numerous breakthroughs in both fundamental science and advanced technology. Accurate identification of spatiotemporal features is a basic requirement for the applications of high-intensity lasers. However, commercial photodetectors (PDs) typically have low saturation intensities and damage thresholds, which necessitates the use of beam splitting or attenuation elements (e.g., glass plates, diffrusers, and filters) in the front of PDs to reduce the laser intensities. Under the excitation of intense field, these optical elements can induce many nonlinear optical effects such as super-continuum spectrum (2), harmonic generation (3), and nonlinear refraction and self-phase modulation (4), thus producing various spatiotemporal distortions ranging from spectral noise (5) to frequency chirping (6) to self-focusing or diverging (7) to beam distortions (8), etc. Therefore, developing strategies for direct photodetection of high-intensity pulsed lasers has long been desired.

As a typical nonlinear optical effect in response to intense laser excitation, multiphoton absorption (MPA) enables sub-bandgap optoelectronics by allowing the simultaneous absorption of multiple photons with energies below the bandgap of optoelectronic materials. This unique process facilitates the development of MPA PDs with extremely high saturation intensities. The MPA PDs based on ZnO (9), MoS<sub>2</sub> (10), and hybrid perovskites (11–15) have demonstrated the

successful applications of two-photon absorption (2PA) and three-photon absorption (3PA) optoelectronics for detecting intense fs lasers. However, the major limitations of current MPA PDs are their short maximum responsive wavelength (shorter than 1.6 μm) and low maximum responsive intensity (lower than 2.5 GW/cm<sup>2</sup>), which mainly arise from the absence of efficient higher-order MPA optoelectronics. Over the past years, considerable efforts have been made to seek innovative MPA materials to address this issue (16–20), but it still remains unattainable.

The optoelectronic properties of perovskites have been intensively investigated in the past decade since the first report on perovskite-based PD (21). Recently, two-dimensional (2D) layered Ruddlesden-Popper (RP) hybrid perovskites, featuring a natural multilayered quantum well (QW) structure with alternating organic layers (barriers) and inorganic sheets (wells) (22), have shown great potential for modulating optical and electronic properties (23–25). The strong quantum and dielectric confinement effects within these QWs result in large exciton binding energies, allowing for formation of room-temperature stable excitons (26). These excitons can serve as a unique type of transition dipoles (27–29) to enhance optical nonlinearities (30). However, realizing the full potential in MPA PDs requires simultaneous optimization of both the MPA nonlinearities of excitons and the electrical properties of carriers. This remains a huge challenge due to the fact that the properties of excitons and carriers are oppositely correlated to the interaction strength of electron-hole pairs (31–33).

In this work, by carefully designing the QW structure of a 2D RP hybrid perovskite, (BA)<sub>2</sub>(MA)<sub>2</sub>Pb<sub>3</sub>Br<sub>10</sub> (BMPB, BA = *n*-butylamine and MA = methylamine), we simultaneously actualize strong high-order MPA nonlinearities and efficient electronic properties. The four-photon absorption (4PA) and five-photon absorption (5PA) coefficients of BMPB are  $9.1 \times 10^{-4} \text{ cm}^5 \text{ GW}^{-3}$  and  $8.7 \times 10^{-5} \text{ cm}^7 \text{ GW}^{-4}$ , respectively, almost 3000 times higher than those of mainstream MPA materials (34–38). This exceptional performance enables

Copyright © 2025 The Authors, some rights reserved; exclusive licensee American Association for the Advancement of Science. No claim to original U.S. Government Works. Distributed under a Creative Commons Attribution License 4.0 (CC BY).

<sup>1</sup>College of Physics and Information Engineering, Fuzhou University, Fuzhou 350108, China. <sup>2</sup>National Laboratory of Solid State Microstructures, School of Electronic Science and Engineering, College of Engineering and Applied Sciences, Nanjing University, Nanjing 210093, China. <sup>3</sup>State Key Laboratory of Structure Chemistry, Fujian Institute of Research on the Structure of Matter, Chinese Academy of Sciences, Fuzhou 350002, China.

\*Corresponding author. Email: longno.2@163.com (J.X.); sunzhihua@fjirm.ac.cn (Z.S.); fsli@fzu.edu.cn (F.L.); linzhou@nju.edu.cn (L.Z.)

†These authors contributed equally to this work.

construction of a BMPB PD for directly detecting high-intensity fs lasers in a broad wavelength-response range of 800 to 2300 nm. This PD also shows a broad intensity-response range, from 1.2 MW/cm<sup>2</sup> to 21.5 GW/cm<sup>2</sup>. Furthermore, it exhibits high-precision imaging capabilities for the intrinsic features of high-intensity fs lasers at different spatial modes, exceeding the performance of Si-based charge-coupled device (CCD). These findings highlight the exceptional potential of high-performance MPA PD for accurately characterizing and imaging high-intensity lasers.

## RESULTS

### Mechanism for exciton-enhanced high-order MPA optoelectronics

To fulfill superior MPA optoelectronics, both efficient high-order MPA nonlinearities and electronic transport properties should be realized. In this case, the primary requirement is the generation of high density of excitons to enhance MPA nonlinearities, as the transition dipole moments of excitons can contribute macroscopic nonlinear optical susceptibility (27–30, 39). The mechanism for MPA

nonlinearities enhanced by exciton dipoles is schematically illustrated in the top of Fig. 1A. Under intense near-infrared (NIR) fs-laser excitation, the valence electrons are excited to the conduction band by simultaneously absorbing multiple NIR photons via virtual intermediate levels, leading to the formation of excitons with pronounced Coulombic interactions. These excitons can act as transition dipoles, providing a large dipole moment (27–29) to facilitate the MPA process of other valence electrons and generating more exciton dipoles. High-density exciton dipoles will strongly enhance the macroscopic nonlinear optical susceptibilities  $\chi^{(n)}$  ( $n=3, 5, 7 \dots$ ) at both lower orders [i.e.,  $\chi^{(3)}$  for 2PA] and higher orders [ $\chi^{(5)}$  for 3PA,  $\chi^{(7)}$  for 4PA, and  $\chi^{(9)}$  for 5PA], respectively. This necessitates a large exciton binding energy to maintain exciton stability at room temperature. The second requirement is the dissociation of a sufficient number of excitons under the applied electric field to ensure efficient electronic transport properties (bottom of Fig. 1A). To ensure efficient exciton dissociation, the ideal structure of MPA material should be featured by moderate dielectric confinement.

Therefore, achieving a strategic trade-off between MPA nonlinearities and electronic transport is crucial for efficient MPA

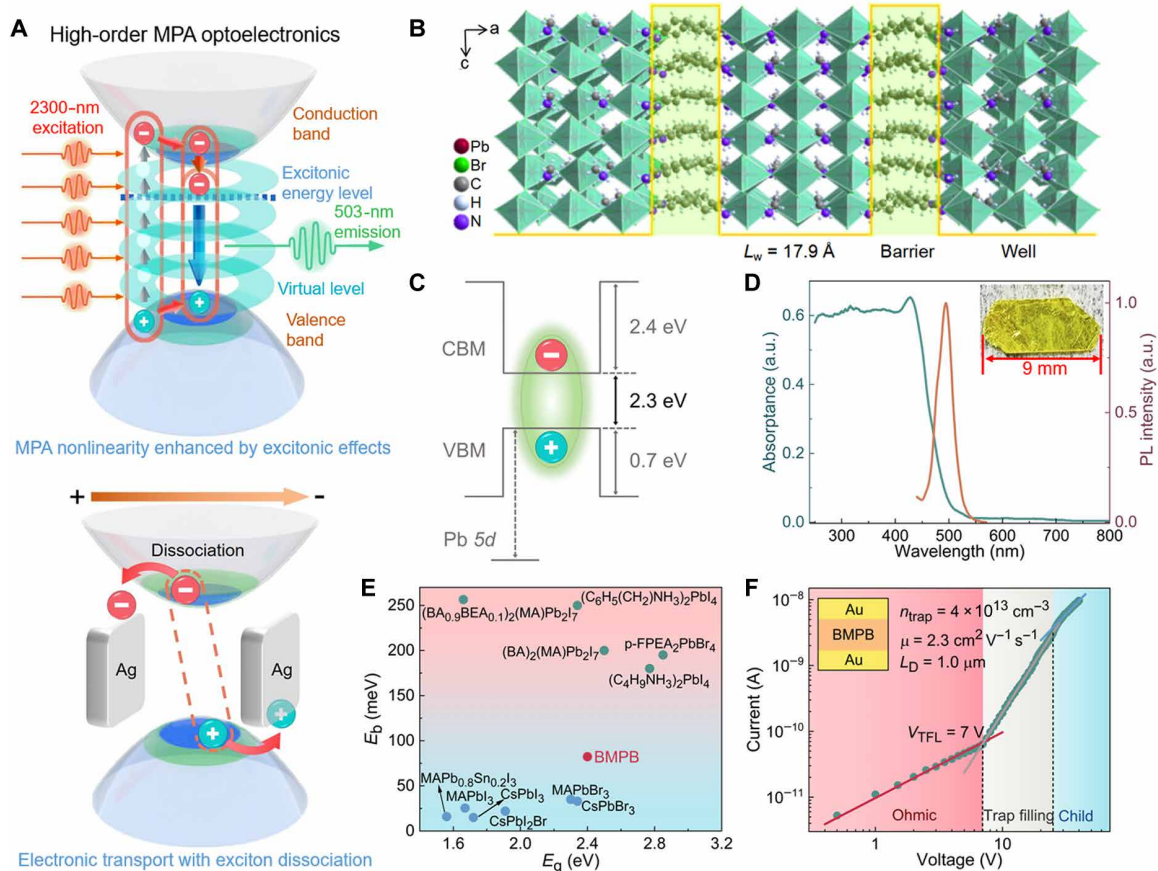


**Fig. 1. The principle of exciton-enhanced MPA optoelectronics and the physical properties of BMPB crystal.** (A) Mechanism of excitonic high-order MPA optoelectronics. Top: Schematic illustration of MPA nonlinearity enhanced by excitonic effects; bottom: schematic diagram of the exciton dissociation and charge transport under bias electric field. (B) Diagram of the crystal structure for top view in *ac* plane. (C) Energy-level scheme evidencing its type-I QW structure. (D) Linear optical absorption and steady-state PL emission spectra. The excitation intensity for PL emission is 14 mW/cm<sup>2</sup> at 405 nm. Inset: Photograph of the as-grown BMPB crystal. (E) Comparison of the exciton binding energies ( $E_b = 82.3$  meV for BMPB) with typical perovskites. References: MAPbI<sub>3</sub> (40), MAPbBr<sub>3</sub> (40), MAPb<sub>0.8</sub>Sn<sub>0.2</sub>I<sub>3</sub> (41), CsPbI<sub>3</sub> (42), CsPbBr<sub>3</sub> (42), (BA)<sub>2</sub>(MA)Pb<sub>2</sub>I<sub>7</sub> (43), (C<sub>4</sub>H<sub>9</sub>NH<sub>3</sub>)<sub>2</sub>PbI<sub>4</sub> (44), p-FPEA<sub>2</sub>PbBr<sub>4</sub> (45), (C<sub>6</sub>H<sub>5</sub>(CH<sub>2</sub>)<sub>2</sub>NH<sub>3</sub>)<sub>2</sub>PbI<sub>4</sub> (25), and (BA<sub>0.9</sub>PEA<sub>0.1</sub>)<sub>2</sub>(MA)Pb<sub>2</sub>I<sub>7</sub> (46). Inset: Diagram of the planar-type device structure used for *I*-*V* measurement. a.u., arbitrary unit. (F) Logarithmic *I*-*V* curve measured by the SCLC model. Inset: Diagram of the planar-type device structure used for *I*-*V* measurement.

photodetection. This indicates that the designing of RP hybrid perovskites should obey the following structural principles: (i) A few-layer inorganic sheets for obtaining strong quantum confinement and a large exciton binding energy. (ii) A suitable dielectric contrast between the inorganic and organic layers (i.e.,  $\epsilon_{\text{inorg}}/\epsilon_{\text{org}}$ ) to achieve moderate dielectric confinement. (iii) Strong interlayer hydrogen bonds for high stability and resistance to damage from high-intensity pulsed lasers.

### Basic characterization of BMPB nonlinear crystal

Based on the above principles, we have designed a RP-type hybrid perovskite, BMPB, in which the inorganic sheets of corner-sharing  $\text{PbBr}_6$  octahedra link to organic BA bilayers via N—H...Br hydrogen bonds along the *a* axis, while  $\text{MA}^+$  cations reside in the perovskite cavities (Fig. 1B). Density functional theory (DFT) calculations reveal that BMPB has a direct bandgap of  $E_g = 2.3$  eV (fig. S1A). Partial density of states analyses indicate that its valence band maximum and conduction band minimum originate from the Br-4p and Pb-6p states, respectively, confirming the role of the inorganic framework in determining its bandgap (fig. S1B). This evidences its type-I quantum structure, with inorganic sheets serving as the wells and organic layers acting as the barriers. The 1.8-nm-thick well layer enables strong quantum confinement (Fig. 1C).

Large BMPB crystals (inset in Fig. 1D) grown from an aqueous solution (see more details in Materials and Methods) show a series of diffraction peaks corresponding to the (200) family of crystal planes in the x-ray diffraction (XRD) pattern (fig. S1C), validating the highly oriented alignment perpendicular to its crystallographic *a* axis and thus high-quality nature of the crystals. The crystals exhibit an absorption cutoff at 520 nm and a sharp photoluminescence (PL) peak around 500 nm (Fig. 1D), closely matching the calculated bandgap. Temperature-dependent PL spectra reveal an exciton binding energy of  $E_b = 82.3$  meV (note S2), which is higher than those of most 3D perovskites (40–42) but lower than those of some mainstream 2D layered perovskites (25, 43–46) (Fig. 1E and table S1). This difference is primarily ascribed to the moderate dielectric contrast between inorganic and organic parts ( $\epsilon_{\text{inorg}}/\epsilon_{\text{org}} = 6.0$  with  $\epsilon_{\text{inorg}} = 32.3$  and  $\epsilon_{\text{org}} = 5.4$ ), larger than those in 3D perovskites but smaller than most 2D perovskite counterparts (47, 48). We anticipate that this strategic modification of excitonic effects will not only stabilize exciton dipoles at room temperature to enhance MPA nonlinearities but also allow the dissociation of abundant excitons under an electric field to enable good charge transport properties.

Ultraviolet photoelectron spectroscopy (49, 50) determines BMPB to be p-type semiconductor (fig. S2). As shown in Fig. 1F, the in-plane carrier diffusion properties of BMPB are determined with a planar-type device structure based on the space charge-limited current (SCLC) method (51). It exhibits three distinct regions in the logarithmic current-voltage (*I*-*V*) curve: linear Ohmic region, trap-filling region, and quadratic Child's region. The trap-state density is estimated to be  $n_{\text{trap}} = 4 \times 10^{13} \text{ cm}^{-3}$  from the trap-filling region, which is three orders of magnitude lower than that of 2D perovskite  $(\text{BA})_2(\text{MA})_3\text{Pb}_4\text{I}_{13}$  ( $\sim 10^{16} \text{ cm}^{-3}$ ) (52) and comparable with that of 3D perovskite  $\text{MAPbBr}_3$  ( $1.1 \times 10^{13} \text{ cm}^{-3}$ ) (53). In the trap-free Child's region, the carrier mobility is derived to be  $\mu = 2.3 \text{ cm}^2 \text{ V}^{-1} \text{ s}^{-1}$ , which surpasses the hybrid perovskite films of  $\text{MAPbI}_3$  ( $1.3 \text{ cm}^2 \text{ V}^{-1} \text{ s}^{-1}$ ) (54) and  $\text{MAPbBr}_3$  ( $0.26 \text{ cm}^2 \text{ V}^{-1} \text{ s}^{-1}$ ) (55). Combined this with the PL lifetime ( $\tau =$

217.2 ns) obtained from the time-resolved PL spectra (fig. S1D), the in-plane diffusion length ( $L_D$ ) is calculated to be  $\sim 1.0 \mu\text{m}$ , which is comparable to those of  $\text{MAPbI}_3$  ( $1.8 \mu\text{m}$ ) (56),  $\text{MAPbBr}_3$  ( $1.3 \mu\text{m}$ ) (56), and  $\text{FAPbI}_3$  crystals ( $1.7 \mu\text{m}$ ) (57), confirming the efficient charge transport properties of BMPB.

### Broadband MPA nonlinearities of BMPB crystal

The MPA nonlinearities of BMPB crystal under broadband fs-laser excitation were studied by measuring the MPA-excited upconversion process. Because of the enhanced excitonic nonlinearities in BMPB, strong *n*PA-excited PL (*n*PPL, *n* = 2, 3, 4, and 5) was observed across a broad NIR range of excitation wavelengths ( $\lambda_{\text{ex}}$ ) from 800 to 2300 nm with the experimental setup presented in Fig. 2A. The recorded PL spectra depending on excitation intensity ( $I_{\text{ex}}$ ) are depicted in Fig. 2B ( $\lambda_{\text{ex}} = 1200, 1850, 2100$ , and 2300 nm) and fig. S5 ( $\lambda_{\text{ex}} = 1300$  and 1750 nm). A gradual red-shift of PL peaks from 486 to 503 nm can be seen with increasing  $\lambda_{\text{ex}}$  due to the reabsorption effect (58, 59). This effect also generates an additional low-energy peak ( $\sim 520$  nm), a phenomenon commonly observed in the MPA-excited PL emission of perovskites (60–62). Furthermore, this peak diminishes as the excitation wavelength increases from 1200 to 2300 nm (Fig. 2B), corresponding to an increase of MPA order from 3PA to 5PA. This behavior can be attributed to the reduction in MPA-induced PL strength, as higher-order MPA nonlinearities significantly lower the MPA excitation efficiency, thereby weakening the reabsorption effect.

From the nonlinear curves of *n*PPL intensity ( $I_{n\text{PPL}}$ ) as a function of  $I_{\text{ex}}$  (Fig. 2C), the fitting slopes in the logarithmic plot meet  $\eta \approx n$  dependence for *n*PA process, in accordance with the power law for perturbative nonlinear process, i.e.,  $I_{n\text{PPL}} \propto I_{\text{ex}}^n$  (see Materials and Methods for theoretical derivation). These results confirm the orders of MPA nonlinearities in BMPB: 2PA at  $\lambda_{\text{ex}} = 800$  nm, 3PA at  $\lambda_{\text{ex}} = 1200$  and 1300 nm, 4PA at  $\lambda_{\text{ex}} = 1750$  and 1850 nm, and 5PA at  $\lambda_{\text{ex}} = 2100$  and 2300 nm, respectively.

Further investigation into the temperature-dependent PL spectroscopy was conducted to determine the exciton-phonon coupling strength (63). As shown in Fig. 2D, the 5PPL spectra ( $\lambda_{\text{ex}} = 2300$  nm) exhibit continuous broadening with increasing the temperature from 133 to 293 K. The exciton-longitudinal optical-phonon coupling strength ( $\Gamma_{\text{LO}}$ ) is derived to be 142.7 meV by fitting the full width at half maximum (FWHM) of variable-temperature 5PPL spectra (Fig. 2E and see note S4 for details). This value is larger than those of typical 3D perovskites such as  $\text{FAPbI}_3$  (34.8 meV) (64) and  $\text{FAPbBr}_3$  (45.4 meV) (65) but smaller than some similar 2D perovskites such as  $(\text{BA})_2(\text{MA})\text{Pb}_2\text{I}_7$  (275 meV) (66) and  $(\text{PEA})_2\text{PbCl}_4$  (261.5 meV) (67). This result indicates a moderate strength of exciton localization within the QWs, which will facilitate the electronic transport of photo-generated carriers.

To quantitatively characterize the MPA performance of BMPB, the open aperture (OA) Z-scan measurement was performed (note S5). The intensity dependence of normalized transmittance is illustrated in Fig. 2F ( $\lambda_{\text{ex}} = 800$  to 2300 nm). The extracted absorption coefficients for each MPA process are listed in Table 1 (see Materials and Methods for details). It can be found that the MPA absorption coefficients of BMPB are notably higher than those of typical inorganic semiconductors and organic chromophores and are comparable with typical all-inorganic or hybrid perovskites (table S2).



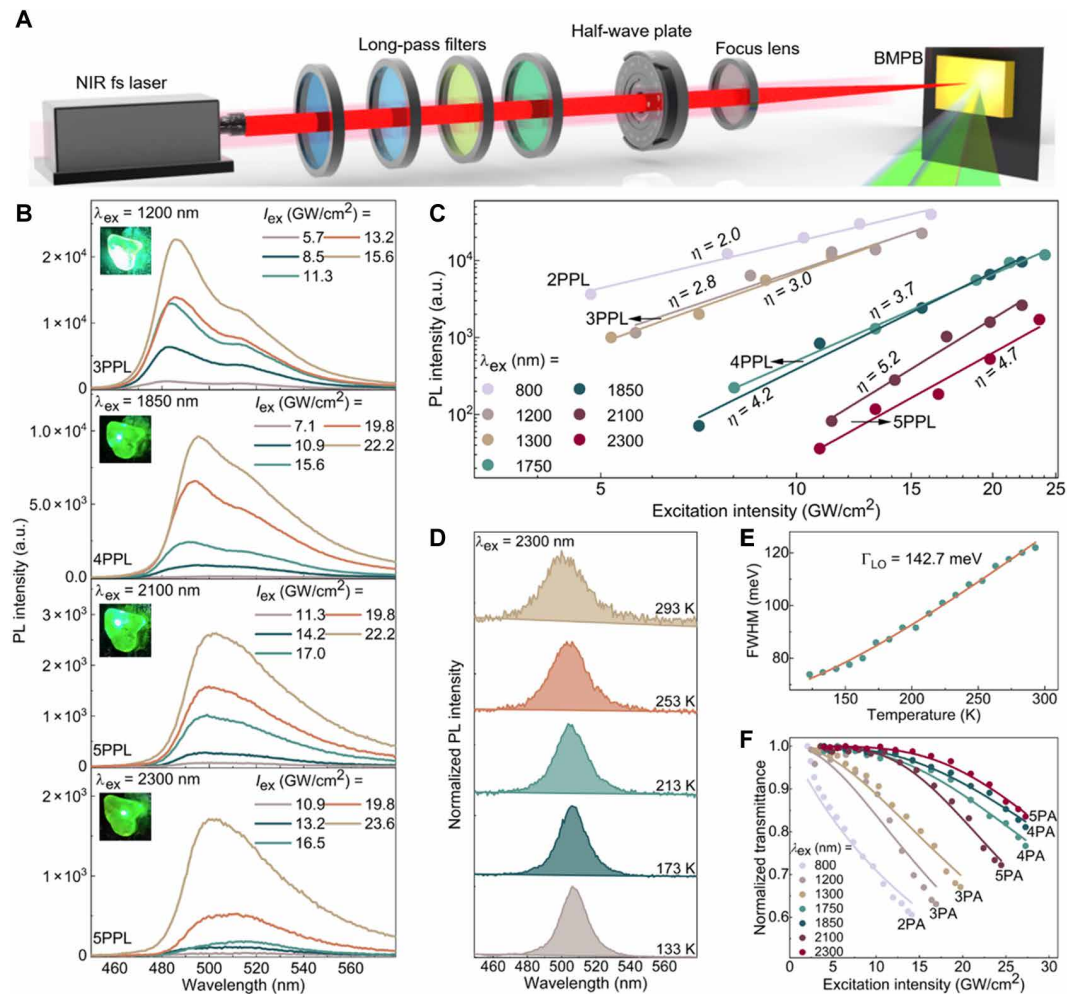


**Fig. 2. MPA nonlinear optical properties of BMPB crystal.** (A) Schematic diagram of the experimental setup for MPA-excited PL measurement. (B) 3PPL ( $\lambda_{ex} = 1200$  nm), 4PPL ( $\lambda_{ex} = 1850$  nm), and 5PPL ( $\lambda_{ex} = 2100$  and  $2300$  nm) spectra at different excitation intensities. Insets: photographs of nPPL emission from BMPB crystal. (C) Logarithmic plot of the nPPL intensity dependence on excitation intensity at different wavelengths. Solid lines: fitting with the power-law relation  $I_{nPPL} \propto I_{ex}^{\eta}$ . (D) Normalized 5PPL spectra measured at five temperatures. (E) FWHM of 5PPL spectra as a function of temperature. Solid line: fitting curves for  $\Gamma_{LO}$  extraction. (F) Normalized transmittance as a function of excitation intensity for 2PA, 3PA, 4PA, and 5PA processes. Solid lines: fitting curves for MPA absorption coefficients.

Table 1. MPA absorption coefficients of BMPB crystal. $\beta$ , $\gamma$ , $\delta$ , and $\varphi$ : 2PA, 3PA, 4PA, and 5PA absorption coefficient, respectively.		
Excitation wavelength (nm)	MPA order	Absorption coefficient
800	2	$\beta = 2.1 \text{ cm GW}^{-1}$
1200	3	$\gamma = 0.11 \text{ cm}^3 \text{ GW}^{-2}$
1300	3	$\gamma = 0.07 \text{ cm}^3 \text{ GW}^{-2}$
1750	4	$\delta = 9.1 \times 10^{-4} \text{ cm}^5 \text{ GW}^{-3}$
1850	4	$\delta = 6.5 \times 10^{-4} \text{ cm}^5 \text{ GW}^{-3}$
2100	5	$\varphi = 8.7 \times 10^{-5} \text{ cm}^7 \text{ GW}^{-4}$
2300	5	$\varphi = 2.2 \times 10^{-5} \text{ cm}^7 \text{ GW}^{-4}$

### MPA-excited sub-bandgap photodetection on broadband fs lasers

The simultaneous realization of strong MPA nonlinearities and efficient electronic transport in BMPB crystal provides opportunities for the direct detection of broadband high-intensity fs lasers. Figure 3A illustrates the as-fabricated PD by transferring 0.8-mm-thick BMPB crystal on a SiO<sub>2</sub> substrate, with a channel length of 1 mm and a width of 5 mm. A fs-laser beam with a diameter of ~0.6 mm was irradiated on the channel. Notably, as depicted in Fig. 3B, the behavior of BMPB PD based on sub-bandgap MPA is quite distinct from that of conventional PDs based on above-bandgap one-photon absorption (1PA). In conventional PDs, the photocurrent ( $I_{ph}$ ) shows a

linear dependence on  $I_{ex}$ , and the responsivity ( $R$ ) remains nearly constant (68, 69) (top of Fig. 3B). In contrast, for MPA PDs, the number of photo-generated carriers increases by the  $n$ -th power with  $I_{ex}$ , leading to nonlinear relationships of  $I_{ph} \propto I_{ex}^n$  and  $R \propto I_{ex}^{n-1}$ . For example, in the case of 2PA photodetection (bottom of Fig. 3B), the number of photo-generated carriers is proportional to  $I_{ex}^2$ , resulting in a quadratic growth of  $I_{ph}$  and a linear growth of  $R$  with  $I_{ex}$ .

The experimentally measured  $I$ - $V$  curves under the excitation of 405-nm continuous-wave laser (for 1PA process) and fs lasers in the range of 800 to 2300 nm (for 2PA-5PA processes) are shown in Fig. 3C (for  $\lambda_{ex} = 2300$  nm) and fig. S9 (for  $\lambda_{ex} = 405, 800, 1300, 1750, 1850$ , and 2100 nm), respectively. The photocurrent shows a

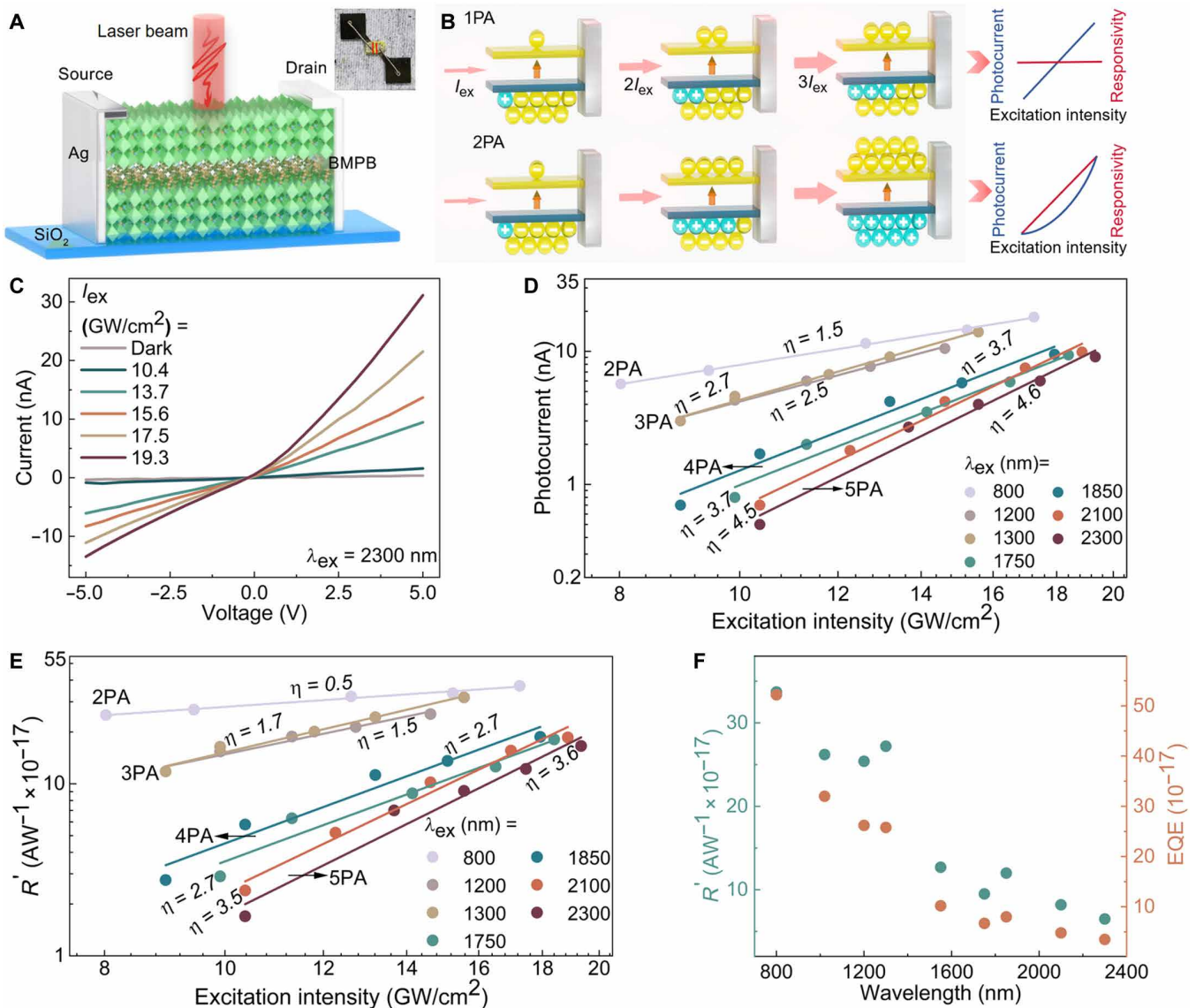


**Fig. 3. MPA-based sub-bandgap photodetection of broadband NIR fs laser based on BMPB crystal.** (A) Schematic illustration of the MPA PD based on BMPB. Inset: photograph of the PD; red solid lines: channel area. (B) Comparison of the photo-carrier generation mechanism between 1PA and 2PA, as well as the photocurrent and responsivity dependence on excitation intensity. (C)  $I$ - $V$  curves measured at different excitation intensities for 5PA ( $\lambda_{ex} = 2300$  nm) photodetection. (D) Logarithmic plot of MPA photocurrent dependence on excitation intensity ( $V_b = 2$  V). Solid lines: fitting with the power-law relation  $I_{ph} \propto I_{ex}^n$ , where the extracted  $n$  meets  $n \approx n$  for  $n$ PA ( $n = 2, 3, 4$ , and  $5$ ). (E) Logarithmic plot of the peak-power responsivity dependence on excitation intensity. Solid lines: fitting with the power-law relation  $R' \propto I_{ex}^{n-1}$ , where the extracted  $n$  meets  $n \approx n - 1$  for  $n$ PA. (F) Peak-power responsivity and EQE dependence on excitation wavelength ( $V_b = 2$  V and  $I_{ex} = 14.2$  GW/cm<sup>2</sup>).

monotonous increase trend with  $I_{\text{ex}}$  due to the combined effects of strong MPA and efficient carrier transport. Furthermore, in the logarithmic plot of  $I_{\text{ph}} \sim I_{\text{ex}}$  under a bias voltage of  $V_b = 2$  V (fig. S10 for  $\lambda_{\text{ex}} = 405$  nm; Fig. 3D for  $\lambda_{\text{ex}} = 800$  to 2300 nm), the fitting slope for  $n$ PA-excited photocurrent is slightly lower than the  $n$  value. This suggests that a portion of carriers recombines during the transport process, while the generation of photocurrent is primarily dominated by MPA effects, consistent with observations reported in other MPA-based photodetection studies (11, 12, 14).

To evaluate the MPA-based photodetection behavior, we described the responsivity ( $R'$ ) related to fs-pulse peak power ( $P_{\text{peak}}$ ) as  $R' = I_{\text{ph}}/P_{\text{peak}}$ . In this sense, the external quantum efficiency (EQE) can be described as  $\text{EQE} = R'hc/q\lambda_{\text{ex}}$ , where  $h$  is Planck's constant,  $c$  is the light speed in vacuum, and  $q$  is the elementary charge. Based on the experimental data in Fig. 3D, the obtained  $R'$  and EQE for each-order MPA process are depicted in Fig. 3E and fig. S11, respectively. The dependence of  $R'$  and EQE on excitation intensity is well described by the power-law relation, i.e.,  $R' \propto I_{\text{ex}}^{n-1}$  and  $\text{EQE} \propto I_{\text{ex}}^{n-1}$ , in

agreement with the aforementioned MPA mechanism. For instance, with  $I_{\text{ex}}$  of 2300-nm fs pulses varying from 10.4 to 19.3 GW/cm<sup>2</sup>,  $R'$  increases from  $1.7 \times 10^{-17}$  to  $1.7 \times 10^{-16}$  AW<sup>-1</sup>, and EQE increases from  $9.0 \times 10^{-18}$  to  $9.0 \times 10^{-17}$ . In addition, with  $\lambda_{\text{ex}}$  increasing from 800 to 2300 nm (under  $V_b = 2$  V and  $I_{\text{ex}} = 14.2$  GW/cm<sup>2</sup>),  $R'$  decreases from  $3.4 \times 10^{-16}$  to  $6.5 \times 10^{-17}$  AW<sup>-1</sup>, and EQE decreases from  $5.2 \times 10^{-16}$  to  $3.5 \times 10^{-17}$  (Fig. 3F). These behaviors mainly arise from the fact that MPA nonlinearities are weakened with increasing MPA orders and excitation wavelengths, in accordance with the variation of absorption coefficients presented in Table 1. Note that the MPA PD performance does not exhibit obvious dependence on BMPB crystal thickness above 0.1 mm nor on light polarization (note S7).

For broadband high-intensity fs-laser photodetection, the intensity- and wavelength-response ranges are the crucial metrics of a MPA PD. Figure 4A depicts the intensity-response spanning of the BMPB PD across the broadband NIR range of 800 to 2300 nm, showing a broad intensity-response range with low thresholds ( $1.2$  MW/cm<sup>2</sup> at  $\lambda_{\text{ex}} = 800$  nm and  $3.2$  MW/cm<sup>2</sup> at  $\lambda_{\text{ex}} = 1020$  nm)

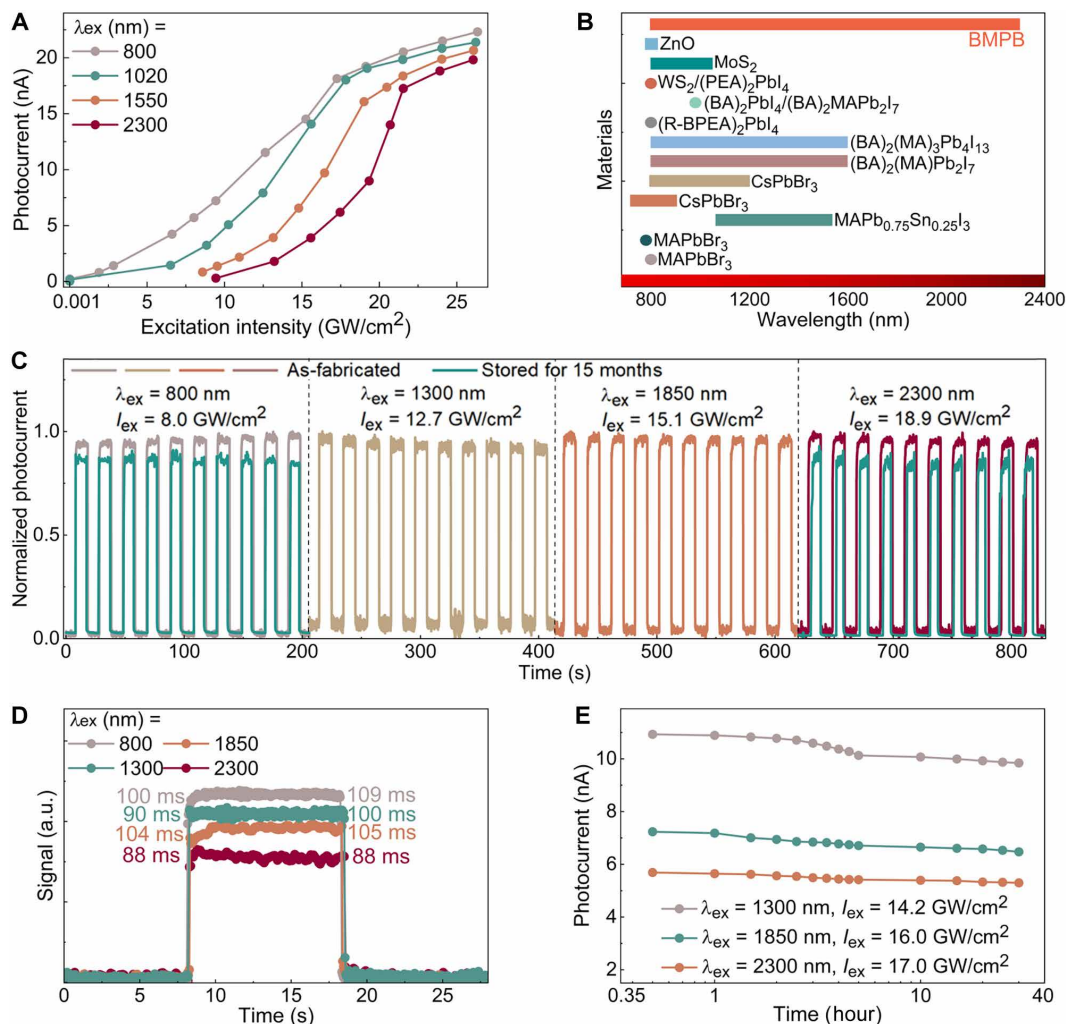


**Fig. 4. Comparison of intensity/wavelength-response range and temporal/stability measurement for BMPB PD.** (A) Photocurrent dependence on excitation intensity at different excitation wavelengths ( $V_b = 2$  V). (B) Wavelength-response range of BMPB compared with some other MPA-based PDs. References: MAPbBr<sub>3</sub> (11), MAPbBr<sub>3</sub> (72), MAPb<sub>0.75</sub>Sn<sub>0.25</sub>I<sub>3</sub> (73), CsPbBr<sub>3</sub> (12), CsPbBr<sub>3</sub> (74), (BA)<sub>2</sub>(MA)<sub>3</sub>PbI<sub>4</sub> (13), (BA)<sub>2</sub>(MA)<sub>3</sub>PbI<sub>4</sub> (13), (R-BPEA)<sub>2</sub>PbI<sub>4</sub> (14), (BA)<sub>2</sub>PbI<sub>4</sub>/(BA)<sub>2</sub>MAPb<sub>2</sub>I<sub>7</sub> (15), WS<sub>2</sub>/(PEA)<sub>2</sub>PbI<sub>4</sub> (75), MoS<sub>2</sub> (10), and ZnO (9). (C) Normalized photocurrent on-off switching cycles ( $V_b = 2$  V) of the as-fabricated BMPB PD ( $\lambda_{\text{ex}} = 800$ , 1300, 1850, and 2300 nm) and stored in a vacuum box for 15 months ( $\lambda_{\text{ex}} = 800$  and 2300 nm). (D) Rise and fall times ( $\lambda_{\text{ex}} = 800$ , 1300, 1850, and 2300 nm) of BMPB PD. (E) Long-term stability of photocurrent at  $\lambda_{\text{ex}} = 1300$ , 1850, and 2300 nm for 30 hours ( $V_b = 2$  V).



and high responsive intensity of  $\sim 21.5 \text{ GW/cm}^2$  across all wavelengths. Furthermore, the intensity-response ranges for different wavelengths are extracted and compared with other representative MPA PDs (fig. S12). The intensity-response threshold at 800 to 1020 nm is significantly lower than the fs-laser-induced retinal damage threshold of  $\sim 10 \text{ MW/cm}^2$  (70, 71), which endows BMPB with great potential for applications in fs-laser safety protection. Note that the threshold measurement at the wavelengths beyond 1020 nm is limited by our fs-laser system: The 800- and 1020-nm pulses are generated by both 80-MHz Ti:sapphire mode-locked oscillator and 5-kHz optical parametric chirped-pulse amplifier (OPCPA), but the 1550- and 2300-nm pulses can only be generated by the high-pulse-energy OPCPA (see more details in Materials and Methods). Therefore, the thresholds for 1550 and 2300 nm maybe much lower than those we measured. Even though, this represents the broadest intensity- and wavelength-response ranges for MPA PDs to the best of our knowledge (9–15, 72–75) (Fig. 4B, fig. S12B, and see the detailed data in tables S3 and S4). The damage threshold as a function of wavelength was measured as shown in fig. S13. The damage threshold slightly decreases from 33.9 to 32.9  $\text{GW/cm}^2$  with increasing the excitation wavelength from 800 to 2300 nm, which may be attributed to the reduction of photon energy.

The temporal photocurrent response and long-time stability are another important metrics for PDs. Under periodic on-off switching of the fs-laser irradiation, the BMPB PD exhibits stable and reproducible photo-switching behavior across the broad NIR range as shown in Fig. 4C ( $\lambda_{\text{ex}} = 800, 1300, 1850$ , and 2300 nm) and fig. S14 ( $\lambda_{\text{ex}} = 1200, 1750$ , and 2100 nm). Both the rise and fall times at all

the wavelengths are  $\sim 100 \text{ ms}$  with minimal fluctuation (Fig. 4D). The large exciton binding energy of BMPB prolongs the exciton lifetime and thus leads to a relatively long response time. The response time is expected to improve by reducing the channel length or by constructing a heterostructure with other band-matched materials.

Figure 4E demonstrates the long-time stability of the BMPB PD over 30 hours under intense fs-laser irradiation with intensity exceeding  $14 \text{ GW/cm}^2$ , without any encapsulation. The absence of noticeable photocurrent degradation suggests its good stability for practical application. In addition, after being stored in a vacuum box for 15 months, this PD still exhibits stable on-off photo-switching behavior. The photocurrent maintains  $\sim 91$  and  $\sim 93\%$  of the initial states at  $\lambda_{\text{ex}} = 800$  and 2300 nm, respectively (Fig. 4C), benefiting from the high-stability structural design of BMPB. Enhanced device stability for practical application will be realizable by encapsulating the PD by polymer film or hexagonal boron nitride (76, 77). Given that perovskite is emerging as a key building block for the next-generation optoelectronics, these excellent performances may boost its potential for high-performance device applications by virtue of the strong high-order MPA optoelectronics.

### Potential applications for accurate imaging of broadband fs lasers

The exceptional photodetection performance of the BMPB PD encourages us to further investigate its practical application in spatial imaging of the broadband high-intensity fs lasers. As illustrated in Fig. 5A, the PD is mounted on a 2D mobile platform, allowing continuous movement in the plane perpendicular to the laser beam

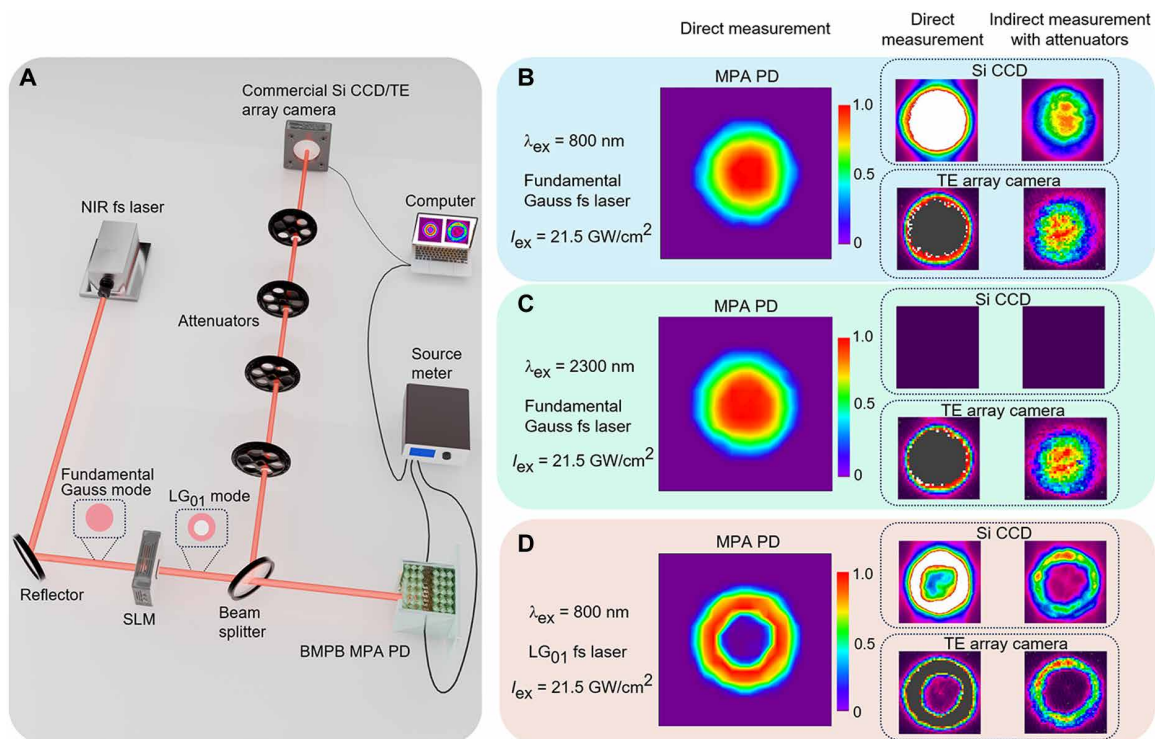


**Fig. 5. Spatial imaging on the broadband NIR fs-laser beams.** (A) Schematic illustration of the imaging system based on either the MPA PD or the commercial imaging device. (B and C) Left: Direct measurement of the fs-laser beam with fundamental Gauss mode through the MPA PD at  $\lambda_{\text{ex}} = 800$  and 2300 nm, respectively. Middle: Direct measurement through the commercial Si CCD or TE array camera at  $\lambda_{\text{ex}} = 800$  and 2300 nm, respectively. Right: Indirect measurement through commercial imaging devices with additional attenuation at  $\lambda_{\text{ex}} = 800$  and 2300 nm, respectively. (D) Direct and indirect measurements of the fs-laser beam with LG<sub>01</sub> mode at  $\lambda_{\text{ex}} = 800 \text{ nm}$ .

(i.e.,  $xy$  plane). The light sources are fs lasers with fundamental Gauss modes at 800 and 2300 nm to verify the broadband imaging capability of the MPA PD. To verify the imaging accuracy of the BMPB PD, the 800-nm fs laser was further modulated into a ring-shaped vortex beam [first-order Laguerre-Gauss ( $LG_{01}$ ) mode] using a spatial light modulator (SLM). The generated photocurrent responding to each spatial position of the laser beam at  $xy$  plane was recorded by a source meter, followed by conversion of the position-resolved photocurrent into a 2D intensity-distribution imaging with  $12 \times 12$  pixels. Figure 5 (B to D) displays the obtained images for the three fs-laser beams, indicating reliable characterization on the intensity distribution of intense fs lasers at different wavelengths and spatial modes, even at intensities up to  $21.5 \text{ GW/cm}^2$ .

For comparison, we used commercial Si-based CCD and  $\text{LiTaO}_3$ -based TE array camera to image the same fs-laser beams with results showed in Fig. 5 (B to D). The Si-based CCD, limited by its low saturation threshold and narrow spectral response, experiences strong response saturation when directly exposed to the high-intensity 800-nm beam and has no response to 2300-nm beam. Although the TE array camera has the good capability in broadband response, it also has strong response saturation, hindering its applications in directly imaging intense fs lasers. To address these issues, a series of optical attenuators are usually placed in the front of these devices. However, as aforementioned, the high-intensity field on the attenuators can excite various nonlinear optical effects and thus introduce severe beam distortions, leading to substantial errors in imaging the intrinsic laser features. The comparison to InGaAs photodiode also verifies the exceptional performance of MPA PD for intense fs-laser imaging at 900 and 1700 nm (note S8). Therefore, the BMPB PD presents an intriguing solution to this long-standing limitation on accurately detecting and imaging strong-field phenomena. Furthermore, enhanced accuracy, resolution, and stability are expected by further fabricating CCD array based on BMPB.

## DISCUSSION

In summary, we have demonstrated a promising pathway for high-precision detection on broadband high-intensity lasers by simultaneously realizing strong high-order MPA nonlinearities and efficient electronic transport properties in the 2D layered hybrid perovskite BMPB. Based on the robust 2PA-5PA optoelectronic performance, the fabricated BMPB PD exhibits a broad high-intensity-response range and high saturation intensities across a broad NIR spectral region (800 to 2300 nm), which surpasses current state-of-the-art PDs. This PD is further applied to accurately image the features of broadband high-intensity fs lasers, highlighting the promising potential of BMPB in CCD-array fabrication with high accuracy and resolution. These findings not only provide a feasible strategy for accurately investigating high-intensity laser field but also expand the potential applications of 2D hybrid perovskites in advanced optoelectronic technologies.

## MATERIALS AND METHODS

### Synthesis and growth of BMPB bulk crystals

During chemical synthesis of BMPB raw material, *n*-butylamine (99%), methylamine (40% in  $\text{H}_2\text{O}$ ), and lead acetate trihydrate [ $\text{Pb}(\text{Ac})_2$ , 99.5%] were stoichiometrically dissolved in the concentrated solution of hydrobromic acid (HBr, 48%). Large-sized

yellow crystals were obtained after 1 week by the temperature cooling method.

### Basic characterization of BMPB crystal

The single crystal x-ray diffraction was performed on Bruker D8 diffractometer with  $\text{Mo K}\alpha$  radiation ( $\lambda = 0.77 \text{ \AA}$ ). Crystal structure of BMPB crystal was solved by the direct method and confirmed by the full-matrix least-squares refinements on  $F^2$  using the SHELXTL software packing. All the non-H atoms were refined anisotropically, and H atoms were generated by geometrical method and refined using the Olex2 software. The linear absorption spectra were measured at room temperature on the PerkinElmer Lambda 900 ultraviolet-visible-NIR spectrometer. The PL measurements were performed on the Edinburgh FLS920 fluorescence spectrometer. For the dielectric constant measurement, silver paste was deposited on the surfaces of the bulk crystals, and the impedance analyses were performed using the TongHui TH2828A impedance analyzer.

### Fabrication of MPA-based PD

The planar-type PD was fabricated on the  $\text{SiO}_2$  substrate, and surface of bulk crystals was cleaned by nitrogen flow beforehand. Silver paste was deposited on the two terminals of crystal surface to form a pair of Ag electrodes. The channel length and width are 1 and 5 mm, respectively. After the preparation of electrodes, the device was annealed at  $70^\circ\text{C}$  in the vacuum atmosphere for 2 hours.

### Steady-state PL measurements

During the 1PPL measurement, a continuous-wave laser ( $\lambda_{\text{ex}} = 405 \text{ nm}$ ) was used as the incident excitation light. For the MPA-related optical measurements, both Ti:sapphire mode-locked oscillator (Chameleon, Coherent;  $\sim 120 \text{ fs}$ , 80 MHz, 680 to 1020 nm) and OPCPA (Topas-C, Coherent; 5 kHz, 800 to 2300 nm) were used as the laser sources. In all the experiments, the crystal samples were rotated repeatedly to ensure the consistency between their  $c$  axes and the polarization direction. The output laser of OPCPA was filtered by suitable long-pass filters to remove the light at undesired wavelengths. Two continuously variable neutral density filters were used to adjust the intensity of excitation laser. For the steady-state PL measurements, a circular lens with the focal length of 80 mm was used to focus the laser vertically onto the bulk crystals with the thickness of  $\sim 0.5 \text{ mm}$ . The PL signals were collected by an optical fiber and coupled to the spectrometer (QE Pro, Ocean Optics) in a reflection spectroscopy geometry. The fiber port was fixed as close as to the sample with a small angle of  $\sim 10^\circ$ . For the temperature-dependent PL measurements, the samples were put in a heating stage, and the temperature was set from 123 to 293 K with the heating rate of  $3.4 \text{ K/min}$ .

### OA Z-scan measurements

The incident laser beam was divided into two parts by a beam splitter. One part was directed into a power detector ( $D_R$ ) as the reference, while the other part was focused onto the bulk crystals (the thickness  $\sim 0.2 \text{ mm}$ ) by a circular lens with the focal length of 200 mm. The beam transmitted through the samples was detected by another power detector ( $D_S$ ) as the signal. The incident beam was propagating along the crystallographic  $a$  axis, and the samples moved along the propagating direction of the beam, i.e.,  $z$  axis. The transmittance was recorded as a function of the sample position ( $z$ ). As the incident power can be regarded as a constant, the sample will be subjected to various peak intensity  $I(z)$  at different position and subsequently



the change of transmittance. The diameters ( $d$ ) of the laser beams at different position were measured through knife-edge scans as shown in fig. S7.

### Photodetection measurements

The  $I$ - $V$  and  $I$ - $t$  measurements on the MPA-based PD were performed using a Keithley 2450 source-meter controlled by the software developed by Wuhan Zeal Young Technology Co. Ltd. A circular lens with the focal length of 200 mm was used to focus the laser vertically onto the device channel. The diameter of the focused laser beam is  $\sim 0.6$  mm.

### Imaging on the broadband fs-laser beams

To characterize the spatial distribution of light intensity for the fs-laser beams with fundamental Gauss mode, the MPA-based PD was fixed on a 2D mobile platform and moved continuously in the plane perpendicular to the fs-laser beam (i.e.,  $xy$  plane). The photocurrent at each point was recorded by a Keithley 2450 source meter, and then the position-resolved photocurrent can be converted into a 2D contrast mapping. For comparison, a commercial InGaAs photodiode (DET10D/M, Thorlabs) was used to measure the position-resolved photo response, and the voltage at each point was recorded by a high-speed oscilloscope (MDO3014, Tektronix). In addition, commercial Si-based CCD (LBP2-IR2, Newport) and LiTaO<sub>3</sub>-based TE array camera (PY-III-C-B, Spiricon) were also used to record the intensity distribution for the fs-laser beams. For the measurement of the fs beam with LG<sub>01</sub> mode, a SLM (F4320, CAS Microstar) was used to convert the fundamental Gauss mode into LG<sub>01</sub> mode.

### Band structure calculations

First-principles DFT calculations were performed using the plane-wave pseudopotential method. The exchange-correlation potential was calculated using Perdew-Burke-Ernzerhof for solids functional within the generalized gradient approximation. The core-electron interactions were described by the norm-conserving pseudopotential.

### Derivation of the MPA strength dependence on excitation intensity

As a nonlinear optical effect, the MPA process can be described by the following expression

$$\frac{dI(z)}{dz} = -\alpha_1 I(z) - \alpha_2 I^2(z) - \alpha_3 I^3(z) - \alpha_4 I^4(z) - \alpha_5 I^5(z) - \dots \quad (1)$$

where  $I(z)$  is the local intensity of incident laser beam propagating along the  $z$ -axis, and  $z$  is the propagation distance of light in the medium. The parameters  $\alpha_1$ ,  $\alpha_2$ ,  $\alpha_3$ ,  $\alpha_4$ , and  $\alpha_5$  are one-, two-, three-, four-, and five-photon absorption coefficients, respectively. At a certain photon frequency  $\nu$ , only the  $n$ PA process satisfying Eq. 1 is available, and then the following relation can be obtained as

$$\frac{dI(z)}{dz} = -\alpha_n I^n(z) \quad (2)$$

The transmitted laser intensity can be obtained by integration of Eq. 2

$$I(L_0) = \frac{I_0}{[1 + (n-1)\alpha_n L_0 I_0^{n-1}]^{1/(n-1)}} \quad (3)$$

where  $I_0$  is the laser intensity at the entrance of the sample and  $L_0$  is the sample thickness. The laser intensity change caused by MPA is as follows

$$\Delta I = I_0 - I(L_0) = I_0 \left\{ 1 - \frac{1}{[1 + (n-1)\alpha_n L_0 I_0^{n-1}]^{1/(n-1)}} \right\} \quad (4)$$

When  $(n-1)\alpha_n L_0 I_0^{n-1} \ll 1$ , an approximation can be made

$$\Delta I \approx (n-1)\alpha_n L_0 I_0^n \quad (5)$$

Since the population of excited-state electrons is proportional to the laser intensity, so if we assume that the MPA-induced PL intensity is proportional to the population of excited-state electrons, then the following relation can be obtained as

$$I_{PL} \propto \Delta I \approx (n-1)\alpha_n L_0 I_0^n \quad (6)$$

This indicates that for  $n$ PA process, the up-conversion PL intensity grows as  $n$ th power with the excitation intensity. At the same time, if we assume that the photocurrent is proportional to the population of excited-state electrons, a similar relation can be obtained as

$$I_{ph} \propto \Delta I \approx (n-1)\alpha_n L_0 I_0^n \quad (7)$$

This suggests that for  $n$ PA photodetection, the photocurrent grows as  $n$ th power with the excitation intensity. Therefore, the responsivity can be expressed as follows

$$R = \frac{I_p}{P} \propto (n-1)\alpha_n L_0 I_0^{n-1} \quad (8)$$

where  $P$  is the incident laser power. This suggests that for  $n$ PA photodetection, the responsivity grows as  $(n-1)$ -th power with the excitation intensity.

For the above-bandgap 1PA photodetection, the linear absorption process can be described as follows

$$\frac{dI(z)}{dz} = -\alpha_1 I(z) \quad (9)$$

The transmitted laser intensity is as follows

$$I(L_0) = I_0 e^{-\alpha_1 L_0} \quad (10)$$

So that the following relation can be obtained as

$$I_{ph} \propto \Delta I = I_0 - I(L_0) = I_0 (1 - e^{-\alpha_1 L_0}) \quad (11)$$

This suggests that for 1PA photodetection, the photocurrent is proportional to the excitation intensity. Further, the responsivity can be obtained as

$$R = \frac{I_p}{P} \propto 1 - e^{-\alpha L_0} \quad (12)$$

This means that for 1PA photodetection, the responsivity is a constant value invariable with the excitation intensity.

### Determination of the MPA absorption coefficients

Based on Eq. 3, the transmittance in  $n$ PA process can be expressed as follows

$$T = \frac{I(L_0)}{I_0} = \frac{1}{[1 + (n-1)\alpha_n L_0 I_0^{n-1}]^{1/(n-1)}} \quad (13)$$

Note that the value of  $I_0$  varies with the position  $z$  along the  $z$ -axis direction, so that the transmittance at the different positions can be measured experimentally. By fitting the experimental data with Eq. 13, the  $n$ PA absorption coefficients can be determined.

## Supplementary Materials

This PDF file includes:

Notes S1 to S8

Figs. S1 to S17

Tables S1 to S4

References

## REFERENCES AND NOTES

- D. E. Spence, P. N. Kean, W. Sibbett, 60-Fsec pulse generation from a self-mode-locked Ti:sapphire laser. *Opt. Lett.* **16**, 42–44 (1991).
- K. Y. Kim, A. J. Taylor, J. H. Glowina, G. Rodriguez, Coherent control of terahertz supercontinuum generation in ultrafast supercontinuum generation in ultrafast laser-gas interactions. *Nat. Photon.* **2**, 605–609 (2008).
- Y.-Y. Lv, J. Xu, S. Han, C. Zhang, Y. Han, J. Zhou, S.-H. Yao, X.-P. Liu, M.-H. Lu, H. Weng, Z. Xie, Y. B. Chen, J. Hu, Y.-F. Chen, S. Zhu, High-harmonic generation in Weyl semimetal  $\beta$ -WP<sub>2</sub> crystals. *Nat. Commun.* **12**, 6437 (2021).
- C. Zhang, H. Wu, Y. Xu, J. Xu, Z. Yan, Y. Hu, Z. Xie, S. Zhu, Plasmon-assisted broadband all-optical control of highly intense femtosecond laser by weak continuous-wave laser. *Adv. Optical Mater.* **8**, 2000560 (2020).
- W. Liu, J. Song, P. Ma, H. Xiao, P. Zhou, Effects of background spectral noise in the phase-modulated single-frequency seed laser on high-power narrow-linewidth fiber amplifiers. *Photonics Res.* **9**, 424–431 (2021).
- J. Mauritsson, P. Johnsson, R. López-Martens, K. Varjú, W. Kornelis, J. Biegert, U. Keller, M. B. Gaarde, K. J. Schafer, A. L'Huillier, Measurement and control of the frequency chirp rate of high-order harmonic pulses. *Phys. Rev. A* **70**, 021801 (2004).
- I. Alexeev, T. M. Antonsen, K. Y. Kim, H. M. Milchberg, Self-focusing of intense laser pulses in a clustered gas. *Phys. Rev. Lett.* **90**, 103402 (2003).
- S. Chang, Off-axial aberrations of a Gaussian beam obliquely passing through a thinradial GRIN lens. *Optik* **126**, 4419–4423 (2015).
- G. Lou, Y. Wu, H. Zhu, J. Li, A. Chen, Z. Chen, Y. Liang, Y. Ren, X. Gui, D. Zhong, Z. Qiu, Z. Tang, S. C. Su, Upconversion single-microbelt photodetector via two-photon absorption simultaneous. *J. Phys. D Appl. Phys.* **51**, 19LT01 (2018).
- F. Zhou, W. Ji, Two-photon absorption and subband photodetection in monolayer MoS<sub>2</sub>. *Opt. Lett.* **42**, 3113–3116 (2017).
- G. Walters, B. R. Sutherland, S. Hoogland, D. Shi, R. Comin, D. P. Sellan, O. M. Bakr, E. H. Sargent, Two-photon absorption in organometallic bromide perovskites. *ACS Nano* **9**, 9340–9346 (2015).
- B. Yang, F. Zhang, J. Chen, S. Yang, X. Xia, T. Pullerits, W. Deng, K. Han, Ultrasensitive and fast all-inorganic perovskite-based photodetector via fast carrier diffusion. *Adv. Mater.* **29**, 1703758 (2017).
- F. Zhou, I. Abdelwahab, K. Leng, K. P. Loh, W. Ji, 2D perovskites with giant excitonic optical nonlinearities for high-performance sub-bandgap photodetection. *Adv. Mater.* **31**, e1904155 (2019).
- Y. Peng, X. Liu, Y. P. Yao, H. Ye, X. Shang, X. Chen, J. Luo, Realization of vis-NIR dual-modal circularly polarized light detection in chiral perovskite bulk crystals. *J. Am. Chem. Soc.* **143**, 14077–14082 (2021).
- J. Wang, Y. Mi, X. Gao, J. Li, J. Li, S. Lan, C. Fang, H. Shen, X. Wen, R. Chen, X. Liu, T. He, D. Li, Giant nonlinear optical response in 2D perovskite heterostructures. *Adv. Optical Mater.* **7**, 1900398 (2019).
- W. Chen, S. Bhaumik, S. A. Veldhuis, G. Xing, Q. Xu, M. Grätzel, S. Mhaisalkar, N. Mathews, T. C. Sum, Giant five-photon absorption from multidimensional core-shell halide perovskite colloidal nanocrystals. *Nat. Commun.* **8**, 15198 (2017).
- X. Zhang, S. Xiao, Z. Guo, B. Yuan, X. Wang, S. Zhang, Y. Shi, T. He, R. Chen, Improving the five-photon absorption from core-shell perovskite nanocrystals. *J. Phys. Chem. Lett.* **14**, 7581–7590 (2023).
- Y. Jiang, K. F. Li, K. Gao, H. Lin, H. L. Tam, Y.-Y. Liu, Y. Shu, K.-L. Wong, W.-Y. Lai, K. W. Cheah, W. Huang, Frequency-upconverted stimulated emission by up to six-photon excitation from highly extended spiro-fused ladder-type oligo(p-phenylene)s. *Angew. Chem. Int. Ed.* **60**, 10007–10015 (2021).
- H. He, Y. Cui, B. Li, B. Wang, C. Jin, J. Yu, L. Yao, Y. Yang, B. Chen, G. Qian, Confinement of perovskite-QDs within a single MOF crystal for significantly enhanced multiphoton excited luminescence. *Adv. Mater.* **31**, 1806897 (2019).
- J. Jiang, G. Niu, L. Sui, X. Wang, X. Zeng, Y. Zhang, L. Che, G. Wu, K. Yuan, X. Yang, Six-photon excited self-trapped excitons photoluminescence in lead-free halide perovskite. *Adv. Optical Mater.* **11**, 2202634 (2023).
- L. Dou, Y. Yang, J. You, Z. Hong, W.-H. Chang, G. Li, Y. Yang, Solution-processed hybrid perovskite photodetectors with high detectivity. *Nat. Commun.* **5**, 5404 (2014).
- E. A. Muljarov, S. G. Tikhodeev, N. A. Gippius, T. Ishihara, Exciton in self-organized semiconductor/insulator superlattices: Pbl-based perovskite compounds. *Phys. Rev. B* **51**, 14370–14378 (1995).
- C. Katan, N. Mercier, J. Even, Quantum and dielectric confinement effects in lower-dimensional hybrid perovskite semiconductors. *Chem. Rev.* **119**, 3140–3192 (2019).
- W. Chen, F. Zhang, C. Wang, M. Jia, X. Zhao, Z. Liu, Y. Ge, Y. Zhang, H. Zhang, Nonlinear photonics using low-dimensional metal-halide perovskites: Recent advances and future challenges. *Adv. Mater.* **33**, 2004446 (2021).
- B. Cheng, T.-Y. Li, P. Maity, P.-C. Wei, D. Nordlund, K.-T. Ho, D.-H. Lien, C.-H. Lin, R.-Z. Liang, X. Miao, I. A. Ajia, J. Yin, D. Sokaras, A. Javey, I. S. Roqan, O. F. Mohammed, J.-H. He, Extremely reduced dielectric confinement in two-dimensional hybrid perovskites with large polar organics. *Commun. Phys.* **1**, 80 (2018).
- J.-C. Blancon, A. V. Stier, H. Tsai, W. Nie, C. C. Stoumpos, B. Traoré, L. Pedesseau, M. Kepenekian, F. Katsutani, G. T. Noe, J. Kono, S. Tretiak, S. A. Crooker, C. Katan, M. G. Kanatzidis, J. J. Crochet, J. Even, A. D. Mohite, Scaling law for excitons in 2D perovskite quantum wells. *Nat. Commun.* **9**, 2254 (2018).
- A. Shimizu, Optical nonlinearity induced by giant dipole moment of Wannier excitons. *Phys. Rev. Lett.* **61**, 613–616 (1988).
- E. Hanamura, Very large optical nonlinearity of semiconductor microcrystallites. *Phys. Rev. B* **37**, 1273–1279 (1988).
- E. Hanamura, Exciton enhancement of optical non-linearity in low-dimensional crystals. *Opt. Quant. Electron.* **21**, 441–450 (1989).
- Y. Gao, N. Q. Huong, J. L. Birman, M. J. Potasek, Large nonlinear optical properties of semiconductor quantum dot arrays embedded in an organic medium. *J. Appl. Phys.* **96**, 4839–4842 (2004).
- O. Voznyy, B. R. Sutherland, A. H. Ip, D. Zhitomirsky, E. H. Sargent, Engineering charge transport by heterostructuring solution-processed semiconductors. *Nat. Rev. Mater.* **2**, 17026 (2017).
- H. Lu, K. Chen, R. S. Bobba, J. Shi, M. Li, Y. Wang, J. Xue, P. Xue, X. Zheng, K. E. Thorn, I. Wagner, C.-Y. Lin, Y. Song, W. Ma, Z. Tang, Q. Meng, Q. Qiao, J. M. Hodgkiss, X. Zhan, Simultaneously enhancing exciton/charge transport in organic solar cells by an organoboron additive. *Adv. Mater.* **34**, e2205926 (2022).
- K. F. Mak, J. Shan, Photonics and optoelectronics of 2D semiconductor transition metal dichalcogenides. *Nat. Photon.* **10**, 216–226 (2016).
- G. S. He, T.-C. Lin, S.-J. Chung, Q. Zheng, C. Lu, Y. Cui, P. N. Prasad, Two-, three-, and four-photon-pumped stimulated cavityless lasing properties of ten stilbazolium-dyes solutions. *J. Opt. Soc. Am. B* **22**, 2219 (2005).
- K. S. Bindra, H. T. Bookey, A. K. Kar, B. S. Wherrett, X. Liu, A. Jha, Nonlinear optical properties of chalcogenide glasses: Observation of multiphoton absorption. *Appl. Phys. Lett.* **79**, 1939–1941 (2001).
- Q. Zheng, H. Zhu, S.-C. Chen, C. Tang, E. Ma, X. Chen, Frequency-upconverted stimulated emission by simultaneous five-photon absorption. *Nat. Photon.* **7**, 234–239 (2013).
- D. Yang, S. Chu, Y. Wang, C. K. Siu, S. Pan, S. F. Yu, Frequency upconverted amplified spontaneous emission and lasing from inorganic perovskite under simultaneous six-photon absorption. *Opt. Lett.* **43**, 2066–2069 (2018).
- D. Yang, C. Xie, X. Xu, P. You, F. Yan, S. F. Yu, Lasing characteristics of CH<sub>3</sub>NH<sub>3</sub>PbCl<sub>3</sub> single-crystal microcavities under multiphoton excitation. *Adv. Optical Mater.* **6**, 1700992 (2018).
- A. Engelmann, V. I. Yudson, P. Peineker, Enhanced optical nonlinearity of hybrid excitons in an inorganic semiconducting quantum dot covered by an organic layer. *Phys. Rev. B* **57**, 1784–1790 (1998).
- A. M. Soufiani, F. Huang, P. Reece, R. Sheng, A. Ho-Baillie, M. A. Green, Polaronic exciton binding energy in iodide and bromide organic-inorganic lead halide perovskites. *Appl. Phys. Lett.* **107**, 231902 (2015).
- K. Galkowski, A. Surrente, M. Baranowski, B. Zhao, Z. Yang, A. Sadhanala, S. Mackowski, S. D. Stranks, P. Plochocka, Excitonic properties of low-band-gap lead-tin halide perovskites. *ACS Energy Lett.* **4**, 615–621 (2019).
- Z. Yang, A. Surrente, K. Galkowski, A. Miyata, O. Portugall, R. J. Sutton, A. A. Haghighirad, H. J. Snaith, D. K. Maude, P. Plochocka, R. J. Nicholas, Impact of the halide cage on the electronic properties of fully inorganic cesium lead halide perovskites. *ACS Energy Lett.* **2**, 1621–1627 (2017).
- Y. Gao, M. Zhang, X. Zhang, G. Lu, Decreasing exciton binding energy in two-dimensional halide perovskites by lead vacancies. *J. Phys. Chem. Lett.* **10**, 3820–3827 (2019).
- Z. Chen, Q. Zhang, M. Zhu, X. Wang, Q. Wang, A. T. S. Wee, K. P. Loh, G. Eda, Q. H. Xu, Synthesis of two-dimensional perovskite by inverse temperature crystallization and studies of exciton states by two-photon excitation spectroscopy. *Adv. Funct. Mater.* **30**, 2002661 (2020).

45. Y. Jiang, M. Cui, S. Li, C. Sun, Y. Huang, J. Wei, L. Zhang, M. Lv, C. Qin, Y. Liu, M. Yuan, Reducing the impact of Auger recombination in quasi-2D perovskite light-emitting diodes. *Nat. Commun.* **12**, 336 (2021).
46. N. Zhou, B. Huang, M. Sun, Y. Zhang, L. Li, Y. Lun, X. Wang, J. Hong, Q. Chen, H. Zhou, The spacer cations interplay for efficient and stable layered 2D perovskite solar cells. *Adv. Energy Mater.* **10**, 1901566 (2020).
47. C. V. V. Ramana, A. B. V. K. Kumar, M. A. Kumar, M. K. Moodley, Dielectric and excess dielectric constants of acetonitrile + butylamine + ethylamine, and + methylamine at 303, 313, and 323 K. *J. Chem.* **2013**, 687106 (2012).
48. M. Sendner, P. K. Nayak, D. A. Egger, S. Beck, C. Müller, B. Epding, W. Kowalsky, L. Kronik, H. J. Snaith, A. Pucci, R. Lovrinčić, Optical phonons in methylammonium lead halide perovskites and implications for charge transport. *Mater. Horiz.* **3**, 613–620 (2016).
49. Y. Li, X. Jiang, Z. Fu, Q. Huang, G.-E. Wang, W.-H. Deng, C. Wang, Z. Li, W. Yin, B. Chen, G. Xu, Coordination assembly of 2D ordered organic metal chalcogenides with widely tunable electronic band gaps. *Nat. Commun.* **11**, 261 (2020).
50. S. Prathapani, P. Bhargava, S. Mallick, Electronic band structure and carrier concentration of formamidinium-cesium mixed cation lead mixed halide hybrid perovskites. *Appl. Phys. Lett.* **112**, 092104 (2018).
51. D. Shi, V. Adinolfi, R. Comin, M. Yuan, E. Alarousu, A. Buin, Y. Chen, S. Hoogland, A. Rothenberger, K. Katsiev, Y. Losovyj, X. Zhang, P. A. Dowben, O. F. Mohammed, E. H. Sargent, O. M. Bakr, Low trap-state density and long carrier diffusion in organolead trihalide perovskite single crystals. *Science* **347**, 519–522 (2015).
52. N. Liu, P. Liu, H. Zhou, Y. Bai, Q. Chen, Understanding the defect properties of quasi-2D halide perovskites for photovoltaic applications. *J. Phys. Chem. Lett.* **11**, 3521–3528 (2020).
53. V. M. L. Corre, E. A. Duijnste, O. E. Tambouli, J. M. Ball, H. J. Snaith, J. Lim, L. J. A. Koster, Revealing charge carrier mobility and defect densities in metal halide perovskites via space-charge-limited current measurements. *ACS Energy Lett.* **6**, 1087–1094 (2021).
54. N. Cho, F. Li, B. Turedi, L. Sinatra, S. P. Sarmah, M. R. Parida, M. I. Saidaminov, B. Murali, V. M. Burlakov, A. Goriely, O. F. Mohammed, T. Wu, O. M. Bakr, Pure crystal orientation and anisotropic charge transport in large-area hybrid perovskite films. *Nat. Commun.* **7**, 13407 (2016).
55. M. I. Saidaminov, V. Adinolfi, R. Comin, A. L. Abdelhady, W. Peng, I. Dursun, M. Yuan, S. Hoogland, E. H. Sargent, O. M. Bakr, Planar-integrated single-crystalline perovskite photodetectors. *Nat. Commun.* **6**, 8724 (2015).
56. M. I. Saidaminov, A. L. Abdelhady, B. Murali, E. Alarousu, V. M. Burlakov, W. Peng, I. Dursun, L. Wang, Y. He, G. Maculan, A. Goriely, T. Wu, O. F. Mohammed, O. M. Bakr, High-quality bulk hybrid perovskite single crystals within minutes by inverse temperature crystallization. *Nat. Commun.* **6**, 7586 (2015).
57. A. Zhumekenov, M. I. Saidaminov, M. A. Haque, E. Alarousu, S. P. Sarmah, B. Murali, I. Dursun, X.-H. Miao, A. L. Abdelhady, T. Wu, O. F. Mohammed, O. M. Bakr, Formamidinium lead halide perovskite crystals with unprecedented long carrier dynamics and diffusion length. *ACS Energy Lett.* **1**, 32–37 (2016).
58. Y. Wang, V. D. Ta, Y. Gao, T. C. He, R. Chen, E. Mutlugun, H. V. Demir, H. D. Sun, Stimulated emission and lasing from CdSe/CdS/ZnS core-multi-shell quantum dots by simultaneous three-photon absorption. *Adv. Mater.* **26**, 2954–2961 (2014).
59. G. S. He, K.-T. Yong, Q. Zheng, Y. Sahoo, A. Baev, A. I. Ryasnyanskiy, P. N. Prasad, Multi-photon excitation properties of CdSe quantum dots solutions and optical limiting behavior in infrared range. *Opt. Express* **15**, 12818–12833 (2007).
60. Y. Yamada, T. Yamada, L. Q. Phuong, N. Maruyama, H. Nishimura, A. Wakamiya, Y. Murata, Y. Kanemitsu, Dynamic optical properties of CH<sub>3</sub>NH<sub>3</sub>PbI<sub>3</sub> single crystals as revealed by one- and two-photon excited photoluminescence measurements. *J. Am. Chem. Soc.* **137**, 10456–10459 (2015).
61. T. Yamada, Y. Yamada, H. Nishimura, Y. Nakaike, A. Wakamiya, Y. Murata, Y. Kanemitsu, Fast free-carrier diffusion in CH<sub>3</sub>NH<sub>3</sub>PbBr<sub>3</sub> single crystals revealed by time-resolved one- and two-photon excitation photoluminescence spectroscopy. *Adv. Electron. Mater.* **2**, 1500290 (2016).
62. T. Yamada, Y. Yamada, Y. Nakaike, A. Wakamiya, Y. Kanemitsu, Photon emission and reabsorption processes in CH<sub>3</sub>NH<sub>3</sub>PbBr<sub>3</sub> single crystals revealed by time-resolved two-photon-excitation photoluminescence microscopy. *Phys. Rev. Appl.* **7**, 014001 (2017).
63. K. Gauthron, J.-S. Lauret, L. Doyennette, G. Lanty, A. A. Choueiry, S. J. Zhang, A. Brehier, L. Largeau, O. Mauguin, J. Bloch, E. Deleporte, Optical spectroscopy of two-dimensional layered (C<sub>6</sub>H<sub>5</sub>C<sub>2</sub>H<sub>4</sub>NH<sub>3</sub>)<sub>2</sub>PbI<sub>4</sub> perovskite. *Opt. Express* **18**, 5912–5919 (2010).
64. H.-H. Fang, F. Wang, S. Adjokatse, N. Zhao, J. Even, M. A. Loi, Photoexcitation dynamics in solution-processed formamidinium lead iodide perovskite thin films for solar cell applications. *Light Sci. Appl.* **5**, e16056 (2016).
65. L. Yang, K. Wei, Z. Xu, F. Li, R. Chen, X. Zhang, X. Cheng, T. Jiang, Nonlinear absorption and temperature-dependent fluorescence of perovskite FAPbBr<sub>3</sub> nanocrystal. *Opt. Lett.* **43**, 122–125 (2018).
66. Y. Liang, Q. Shang, Q. Wei, L. Zhao, Z. Liu, J. Shi, Y. Zhong, J. Chen, Y. Gao, M. Li, X. Liu, G. Xing, Q. Zhang, Lasing from mechanically exfoliated 2D homologous Ruddlesden-Popper perovskite engineered by inorganic layer thickness. *Adv. Mater.* **31**, e1903030 (2019).
67. P. Cai, Y. Huang, H. J. Seo, Anti-stokes ultraviolet luminescence and exciton detrapping in the two-dimensional perovskite (C<sub>6</sub>H<sub>5</sub>C<sub>2</sub>H<sub>4</sub>NH<sub>3</sub>)<sub>2</sub>PbCl<sub>4</sub>. *J. Phys. Chem. Lett.* **10**, 4095–4102 (2019).
68. H. Kind, H. Yan, B. Messer, M. Law, P. Yang, Nanowire ultraviolet photodetectors and optical switches. *Adv. Mater.* **14**, 158–160 (2002).
69. S.-C. Kung, W. E. van der Veer, F. Yang, K. C. Donovan, R. M. Penner, 20 μs Photocurrent response from lithographically patterned nanocrystalline cadmium selenide nanowires. *Nano Lett.* **10**, 1481–1485 (2010).
70. L. N. McLin, A case study of a bilateral femtosecond laser injury, in *ILSC 2013: Proceedings of the International Laser Safety Conference* (AIP Publishing; 2013), pp. 223–227.
71. B. A. Rockwell, R. J. Thomas, A. Vogel, Ultrashort laser pulse retinal damage mechanisms and their impact on thresholds. *Med. Laser Appl.* **25**, 84–92 (2010).
72. B. Yang, J. Chen, Q. Shi, Z. Wang, M. Gerhard, A. Dobrovolsky, I. G. Scheblykin, K. J. Karki, K. Han, T. Pullerits, High resolution mapping of two-photon excited photocurrent in perovskite microplate photodetector. *J. Phys. Chem. Lett.* **9**, 5017–5022 (2018).
73. Y. Xie, J. Fan, C. Liu, S. Chi, Z. Wang, H. Yu, H. Zhang, Y. Mai, J. Wang, Giant two-photon absorption in mixed halide perovskite CH<sub>3</sub>NH<sub>3</sub>Pb<sub>0.75</sub>Sn<sub>0.25</sub>I<sub>3</sub> thin films and application to photodetection at optical communication wavelengths. *Adv. Optical Mater.* **6**, 1700819 (2018).
74. J. Song, Q. Cui, J. Li, J. Xu, Y. Wang, L. Xu, J. Xue, Y. Dong, T. Tian, H. Sun, H. Zeng, Ultralarge all-inorganic perovskite bulk single crystal for high-performance visible-infrared dual-modal photodetectors. *Adv. Optical Mater.* **5**, 1700157 (2017).
75. Q. Wang, A. T. S. Wee, Upconversion photovoltaic effect of WS<sub>2</sub>/2D perovskite heterostructures by two-photon absorption. *ACS Nano* **15**, 10437–10443 (2021).
76. F. Li, C. Ma, H. Wang, W. Hu, W. Yu, A. D. Sheikh, T. Wu, Ambipolar solution-processed hybrid perovskite phototransistors. *Nat. Commun.* **6**, 8238 (2015).
77. H.-C. Cheng, G. Wang, D. Li, Q. He, A. Yin, Y. Liu, H. Wu, M. Ding, Y. Huang, X. Duan, van der Waals Heterojunction devices based on organohalide perovskites and two-dimensional materials. *Nano Lett.* **16**, 367–373 (2016).
78. N. F. Mott, R. W. Gurney, *Electronic processes in ionic crystals* (Clarendon Press, 1948).
79. S. Sun, T. Salim, N. Mathews, M. Duchamp, C. Boothroyd, G. Xing, T. Z. Sum, Y. M. Lam, The origin of high efficiency in low-temperature solution-processable bilayer organometal halide hybrid solar cells. *Energ. Environ. Sci.* **7**, 399–407 (2014).
80. J. Lee, E. S. Koteles, M. O. Vassell, Luminescence linewidths of excitons in GaAs quantum wells below 150 K. *Phys. Rev. B* **33**, 5512–5516 (1986).
81. S. Rudin, T. L. Reinecke, B. Segall, Temperature-dependent exciton linewidths in semiconductors. *Phys. Rev. B* **42**, 11218–11231 (1990).
82. X. B. Zhang, T. Taliercio, S. Kolliakos, P. Lefebvre, Influence of electron-phonon interaction on the optical properties of III nitride semiconductors. *J. Phys. Condens. Matter* **13**, 7053–7074 (2001).
83. A. D. Wright, C. Verdi, R. L. Milot, G. E. Eperon, M. A. Pérez-Osorio, H. J. Snaith, F. Giustino, M. B. Johnston, L. M. Herz, Electron-phonon coupling in hybrid lead halide perovskites. *Nat. Commun.* **7**, 11755 (2016).
84. D. Yang, C. Xie, J. Sun, H. Zhu, X. Xu, P. You, S. P. Lau, F. Yan, S. F. Yu, Amplified spontaneous emission from organic-inorganic hybrid iodide perovskite single crystals under direct multiphoton excitation. *Adv. Optical Mater.* **4**, 1053–1059 (2016).
85. Z. Liu, Z. Hu, Z. Zhang, J. Du, J. Yang, X. Tang, W. Liu, Y. Leng, Two-photon pumped amplified spontaneous emission and lasing from formamidinium lead bromine nanocrystals. *ACS Photonics* **6**, 3150–3158 (2019).
86. F. Zhao, J. Li, X. Gao, X. Qiu, X. Lin, T. He, R. Chen, Comparison studies of the linear and nonlinear optical properties of CsPbBr<sub>3-x</sub> nanocrystals: The influence of dimensionality and composition. *J. Phys. Chem. C* **123**, 9538–9543 (2019).
87. Y. Wang, X. Li, X. Zhao, L. Xiao, H. Zeng, H. Sun, Nonlinear absorption and low-threshold multiphoton pumped stimulated emission from all-inorganic perovskite nanocrystals. *Nano Lett.* **16**, 448–453 (2016).
88. J. Li, C. Ren, X. Qiu, X. Lin, R. Chen, C. Yin, T. He, Ultrafast optical nonlinearity of blue-emitting perovskite nanocrystals. *Photonics Res.* **6**, 554–559 (2018).
89. R. Ketavath, N. K. Katturi, S. G. Ghugal, H. K. Kolli, T. Swetha, V. R. Soma, B. Murali, Deciphering the ultrafast nonlinear optical properties and dynamics of pristine and Ni-doped CsPbBr<sub>3</sub> colloidal two-dimensional nanocrystal. *J. Phys. Chem. Lett.* **10**, 5577–5584 (2019).
90. J. He, W. Ji, J. Mi, Y. Zhang, J. Y. Ying, Three-photon absorption in water-soluble ZnS nanocrystals. *Appl. Phys. Lett.* **88**, 181114 (2006).
91. X. Qiu, J. Hao, J. Li, Z. Gong, S. Li, J. Cheng, X. Lin, T. He, Strong multiphoton absorption in chiral CdSe/CdS dot/rod nanocrystal-doped poly(vinyl alcohol) films. *Opt. Lett.* **44**, 2256–2259 (2019).
92. F. E. Hernández, K. D. Belfield, I. Cohanoschi, M. Balu, K. J. Schafer, Three- and four-photon absorption of a multiphoton absorbing fluorescent probe. *Appl. Optics* **43**, 5394–5398 (2004).

#### Acknowledgments

**Funding:** This work is supported by the National Key R&D Program of China grants



2021YFA1400700 (to L.Z.) and 2022YFB3606500 (to F.L.); the National Natural Science Foundation of China grants 62375122 (to J.X.), 12334015 (to J.X.), 22125110 (to Z.S.), and 92150302 (to J.X.); the Fujian Science & Technology Innovation Laboratory for Optoelectronic Information of China grant 2021ZZ126 (to F.L.); and Natural Science Foundation of Jiangsu Province grant BK20243009 (to L.Z.). **Author contributions:** Discovery and ideation were by J.X., Z.S., S.Z., and L.Z. Experiments were carried out by Y.X., H.X., P.Z., and J.X. Analysis and simulations were conducted by Y.X., H.X., and J.X. Writing was done by Y.X. and J.X. Review and editing was done by Z.S., F.L., and L.Z. All authors contributed to the discussion of results.

**Competing interests:** The authors declare that they have no competing interests. **Data and materials availability:** All data needed to evaluate the conclusions in the paper are present in the paper and/or the Supplementary Materials.

Submitted 19 October 2024

Accepted 18 April 2025

Published 23 May 2025

10.1126/sciadv.adt9952